Supporting Information

Schottky junction with Bi/Bi_2O_3 core-shell nanoparticles modified g-C_3N_4 for boosting photocatalytic H_2O_2 evolution from pure water

Xinyue Yan,[†a] Guiyang Yu,[†b]* Chuanwang Xing,[a] Yujia Hu,[a] Heyuan Liu[c] and Xiyou Li[a]*

[a] School of Materials Science and Engineering, China University of Petroleum (East China), Qingdao, Shandong, 266580, PR China

[b] Key Laboratory of Optic-electric Sensing and Analytical Chemistry for Life Science (MOE), College of Chemistry and Molecular Engineering, Qingdao University of Science and Technology, Qingdao 266042, PR China.

[c] College of New Energy, China University of Petroleum (East China), Qingdao, Shandong, 266580, PR China

* Corresponding author.

Emails: xiyouli@upc.edu.cn; yugy3413@qust.edu.cn

[†] Xinyue Yan and Guiyang Yu contributed equally.

Contents:

Experimental section

Fig. S1 Zeta potentials of pristine g-C_3N_4 in pure water.

Fig. S2 (a) SEM and (b) TEM images of pristine g-C_3N_4.

Fig. S3 (a) SEM and (b) corresponding magnified region images of 2% Bi/Bi_2O_3@g-C_3N_4.

Fig. S4 (a, b) TEM and (c) HRTEM images of 2% Bi/Bi_2O_3@g-C_3N_4.

Fig. S5 EDS mapping images of 2% Bi/Bi_2O_3@g-C_3N_4.

Fig. S6 (a) XRD patterns of original and retested 2% Bi/Bi_2O_3@g-C_3N_4 samples. (b) HRTEM and corresponding magnified region images of 2% Bi/Bi_2O_3@g-C_3N_4.

Fig. S7 FTIR spectra of g-C_3N_4, and various Bi/Bi_2O_3@g-C_3N_4 samples.

Fig. S8 (a) N_2 adsorption-desorption isotherms of g-C_3N_4, and various Bi/Bi_2O_3@g-C_3N_4 samples. (b) Pore size distribution curves of g-C_3N_4 and 2% Bi/Bi_2O_3@g-C_3N_4 samples.

Fig. S9 XPS survey spectra of g-C_3N_4, and 2% Bi/Bi_2O_3@g-C_3N_4 samples.

Fig. S10 UV-Vis diffuse reflectance spectra of g-C_3N_4, and various Bi/Bi_2O_3@g-C_3N_4 samples.

Fig. S11 Mott-Schottky plot of (a) g-C_3N_4 and (b) Bi/Bi_2O_3 at different frequencies.

Fig. S12 (a) DFT calculations for the molecular orbits of g-C_3N_4 model (Yellow and blue isosurfaces represent electron accumulation and electron depletion, respectively). Density of states (DOS) of g-C_3N_4 model: (b) sum, (c) N and (d) C elements.

Fig. S13 Bi 4f XPS spectra of 2% Bi/Bi_2O_3@g-C_3N_4 samples in dark, light irradiation for 5 min and 20 min.

Fig. S14 (a) PL spectra and (b) decay curves of g-C_3N_4, and various Bi/Bi_2O_3@g-C_3N_4 samples.

Fig. S15 Time-dependent photocurrent responses of g-C_3N_4, and various Bi/Bi_2O_3@g-C_3N_4 samples.

Fig. S16 Standard curve of H_2O_2 evolution amount.

Fig. S17 XRD patterns of fresh and used 2% Bi/Bi_2O_3@g-C_3N_4 samples under the dried temperature of (a) 80 ºC and (b) 50 ºC.

Fig. S18 FTIR spectra of fresh and used 2% Bi/Bi_2O_3@g-C_3N_4 samples.

Fig. S19 (a) C 1s, (b) N 1s, (c) Bi 4f, and (d) O 1s spectra of fresh and used 2% Bi/Bi_2O_3@g-C_3N_4 samples.

Fig. S20 (a) Time course of photocatalytic H_2O_2 production and (b) H_2O_2 production rate for g-C_3N_4, 2% Bi/Bi_2O_3@g-C_3N_4 and 2% Bi/Bi_2O_3@g-C_3N_4-Mix samples under pure water.

Fig. S21 (a) Time course of photocatalytic H_2O_2 production and (b) H_2O_2 production rate for 2% Bi@g-C_3N_4, 2% Bi_2O_3@g-C_3N_4 and 2% Bi/Bi_2O_3@g-C_3N_4 samples under pure water.

Fig. S22 (a) UV-Vis diffuse reflectance spectra (inset is plots of transformed Kubelka–Munk function versus photon energy), (b) VB-XPS spectra of Bi_2O_3.

Fig. S23 (a) PL emission spectra and (b) photocurrent curves for 2% Bi@g-C_3N_4, 2% Bi_2O_3@g-C_3N_4 and 2% Bi/Bi_2O_3@g-C_3N_4 samples.

Fig. S24 (a) Zero-order kinetic fitting curves (b, c) first-order kinetic fitting curves of g-C_3N_4, and various Bi/Bi_2O_3@g-C_3N_4 samples.

Fig. S25 Time course of photocatalytic H_2O_2 production over 2% Bi/Bi_2O_3@g-C_3N_4 with different quenchers.

Fig. S26 Comparison of Zeta potentials over pristine g-C_3N_4 and various Bi/Bi_2O_3@g-C_3N_4 samples in pure water.

Fig. S27 The first derivative curve of the relationship between $\Delta E/\Delta V$ and titration volume using 10^{-5} mol/L NaOH as the titrant upon g-C_3N_4 and 2% Bi/Bi_2O_3@g-C_3N_4 samples based on potentiometric titration method.

Table S1 The element content of g-C_3N_4 and 2% Bi/Bi_2O_3@g-C_3N_4 based ICP analysis.

Table S2 The absolute fluorescence quantum yield (%) of g-C_3N_4 and Bi/Bi_2O_3@g-C_3N_4 samples excited at 340 nm in the wavelength range of 390-550 nm.

Table S3 Time constant τ of fluorescence decay curves of g-C_3N_4 and Bi/Bi_2O_3@g-C_3N_4 samples.

Table S4 Comparison of H_2O_2 production performance of different photocatalysts.

Reference

Experimental section

Chemicals

Melamine, $Bi(NO_3)_3 \cdot 5H_2O$ (99.0%), Polyvinylpyrrolidone (PVP, MW≈ 58,000 g/mol), Ethylene glycol ($C_2H_6O_2$, 99.0%), Metal Bi (CAS: 7440-69-9), and Ethanol (CH_3CH_2OH, 99.5%) were purchased from Aladdin. Deionized water was used to prepare all solutions and to rinse samples and glassware.

Characterization

X-ray diffraction (XRD) patterns of these nanocomposites were obtained by Rigaka Ultima IV diffractometer with Cu Kα radiation (λ = 0.1538 nm). The molecular structure was measured by Fourier transform infrared（FTIR）spectra on a Hitachi U-3300 Fourier infrared spectrometer. The surface morphology and structure were investigated by using Field-emission scanning electron microscope (SEM) (JEOL JSM-6700F) and transmission electron microscope (TEM) (JEM 2100). The Brunauer–Emmett–Teller (BET) specific surface area and pore size distribution were derived from Beckman Coulter SA3100 analyzer. The N_2 adsorption-desorption isotherm was measured at 77 K. The samples were pretreated and degassed under vacuum at 120℃. The optical properties were recorded in the 300-800 nm range on a Hitachi UH-4150 spectrophotometer using $BaSO_4$ as a background. Ultraviolet photoelectron spectroscopy (UPS) was tested by X-ray photoelectron spectrometer (ThermoFisher, ESCALAB 250 Xi). Among them, the vacuum degree of the analysis chamber is 8×10^{-10} Pa, and Hel 21.22 eV is used for testing. The energy resolution is 90-120 meV and the light spot is 1 mm. The surface chemical states of samples were investigated by X-

ray photoelectron spectroscopy (XPS) using Thermo Escalab 250Xi with Al Kα as excitation source. The sample was etched and thinned using an argon ion gun. The etching spot size was 1.5mm, the depth was 30 nm, and the etching voltage was 3000 eV. Steady-state photoluminescence (PL) spectra, time-resolved photoluminescence spectra and photoluminescence quantum yields were captured on a FLS980 fluorescence spectrophotometer (Edinburgh) with an excitation of 340 nm.

Photocatalytic production of H_2O_2 experiment

The specific steps of the photocatalytic production of hydrogen peroxide experiment are as follows: First, evenly disperse 50 mg catalyst in 50 mL water and put it into a quartz glass reactor with temperature-controlled circulating water device. Then, under dark conditions, the system was constantly bubbled O_2 and stirred for 1 h to achieve the adsorption-desorption equilibrium before the reaction. Finally, the suspension was irradiated under a 300 W xenon lamp equipped with a 420 nm cut-off filter, and 2 mL solution was taken at intervals. The catalyst powder was filtered and removed by a 0.22 um filter, and the concentration of hydrogen peroxide was measured by iodimetry. In addition, the decomposition behavior of hydrogen peroxide at an initial concentration of 1 mM was studied in open air. In order to study the stability and recyclability of the photocatalyst, the reaction solution was recovered, washed with deionized water and ethanol, and then dried for circulation experiment.

The apparent quantum efficiency (AQE) was carried out under the same photocatalytic conditions, except for the irradiation light wavelength obtained by changing a band pass optical filter and using 50 mg catalyst. AQE was calculated using

the following formula:

$$AQE = \frac{number\ of\ reacted\ electrons}{number\ of\ incident\ photos} \times 100\%$$

$$= \frac{2 \times number\ of\ evolved\ H_2O_2 molecules}{number\ of\ incident\ photos} \times 100\%$$

Electrochemical and Photoelectrochemical measurements

Rotating disk electrode (RDE) was measured in a conventional three-electrode battery system on CHI 760E (Shanghai, Chenhua) electrochemical workstation. The RDE consists of a working electrode, an Ag/AgCl reference electrode and a carbon rod pair electrode. The working electrode was prepared as follows: 5 mg catalyst powder was dispersed in 800 μL anhydrous ethanol and 30 μL Nafion (5 wt%, Sigma-Aldrich), then then ultrasonic treatment to form a uniform suspension. 10μL suspension was uniformly dropped on the glassy carbon electrode and dried at room temperature. Linear sweep voltammetry (LSV) curves were collected at a scan rate of 10 mV s^{-1} in an O_2-saturated 0.1 mmol L^{-1} phosphate buffer solution (pH=7). The average number of electrons (n) involved in the total reduction of O_2 was obtained by linear regression of the plots using the following formula:

$$j^{-1} = j_k^{-1} + B^{-1}\omega^{-1/2}$$

$$B = 0.2nFv^{-1/6}CD^{2/3}$$

Where j is the measured current density, j_k is the kinetic current density, ω is the rotating speed (rpm), F is the Faraday constant (96,485 C mol^{-1}), v is the kinetic viscosity of water (0.01 cm^2 s^{-1}), C is the bulk concentration of O_2 in water (1.26×10^{-3} mol cm^{-3}), and D is the diffusion coefficient of O_2 (2.7×10^{-5} cm^2 s^{-1}), respectively.

The transient photocurrent response and electrochemical impedance spectra (EIS) were recorded with a CHI760D electrochemical workstation (Shanghai Chenhua Instrument Corp., China) in a conventional three-electrode system consisting of carbon rod counter electrode, Ag/AgCl reference electrode and working electrode. First of all, the sample (2 mg) was uniformly dispersed in 1 mL anhydrous ethanol and treated by ultrasound for 2 hours to form a uniform suspension. The working electrode is made by dropping suspended solution onto a pre-cleaned FTO glass surface and dried at room temperature. During the measurement, three electrodes were immersed in 0.5 M Na_2SO_4 aqueous solution and the working electrodes were illuminated by a 300 W Xe lamp with a 420 nm cut-off filter. The electrochemical impedance spectroscopy (EIS) was collected on a frequency between 10^{-2} and 10^5 Hz. Moreover, Mott-Schottky curves were also collected at the frequency of 500 Hz and 1000 Hz.

Theoretical calculations

All of calculations were performed with Cambridge Serial Total Energy Package (CASTEP) plane-wave code in Material Studio software based on density functional theory (DFT) [1-2]. The generalized gradient approximation (GGA) in the scheme of the Perdew-Burke-Ernzerhof (PBE) was employed as exchange-correlation functional. The geometry structures were optimized with the cutoff energy of 400 eV [3]. In order to describe the van der Waals (vdW) interaction of the system properly, TS method of DFT-D was applied [4]. The SCF tolerance was set to 10^{-5} eV and the Koelling-Harmon relativistic treatment was used for scalar relativistic corrections to heavy element.

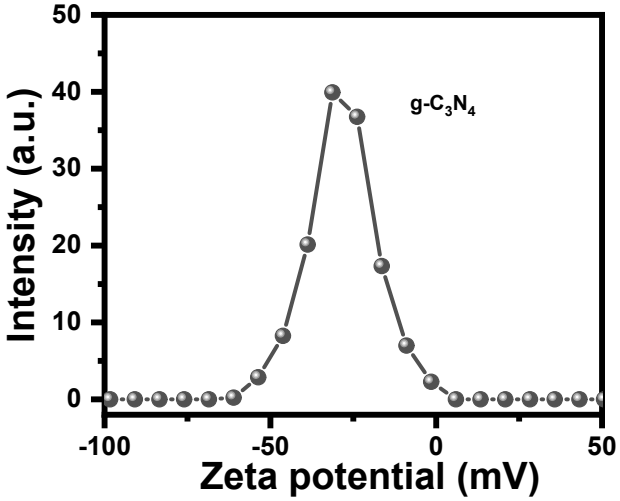

Fig. S1 Zeta potentials of pristine g-C_3N_4 in pure water.

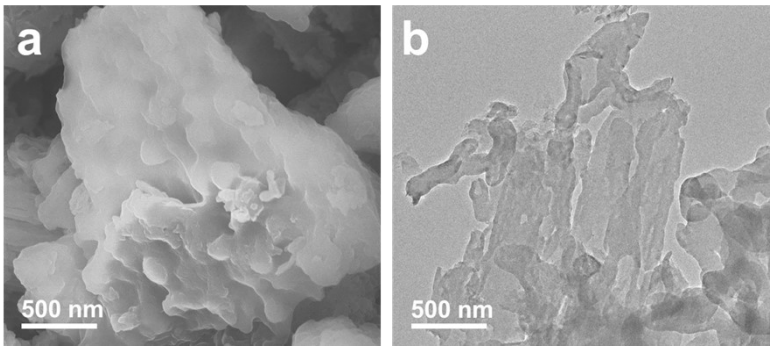

Fig. S2 (a) SEM and (b) TEM images of pristine g-C_3N_4.

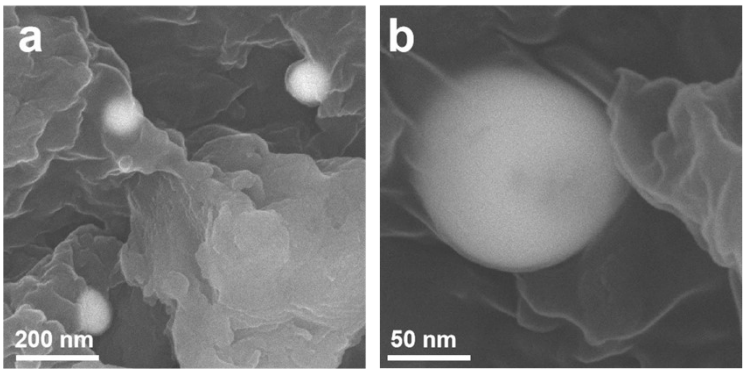

Fig. S3 (a) SEM and (b) corresponding magnified region images of 2% Bi/Bi_2O_3@g-C_3N_4.

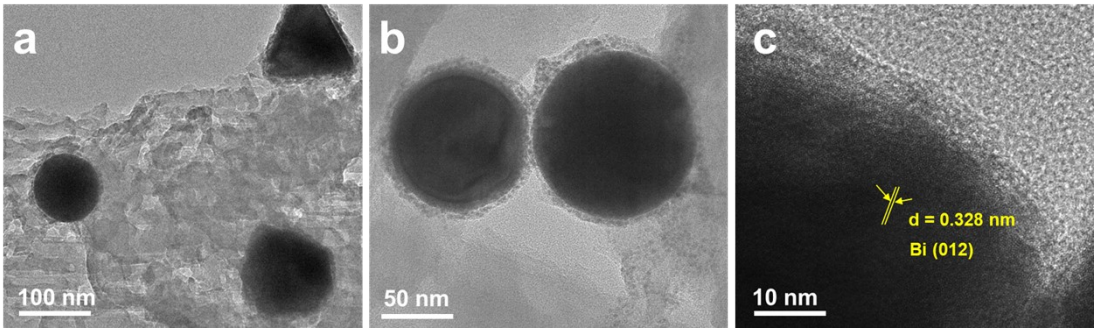

Fig. S4 (a, b) TEM and (c) HRTEM images of 2% Bi/Bi_2O_3@g-C_3N_4.

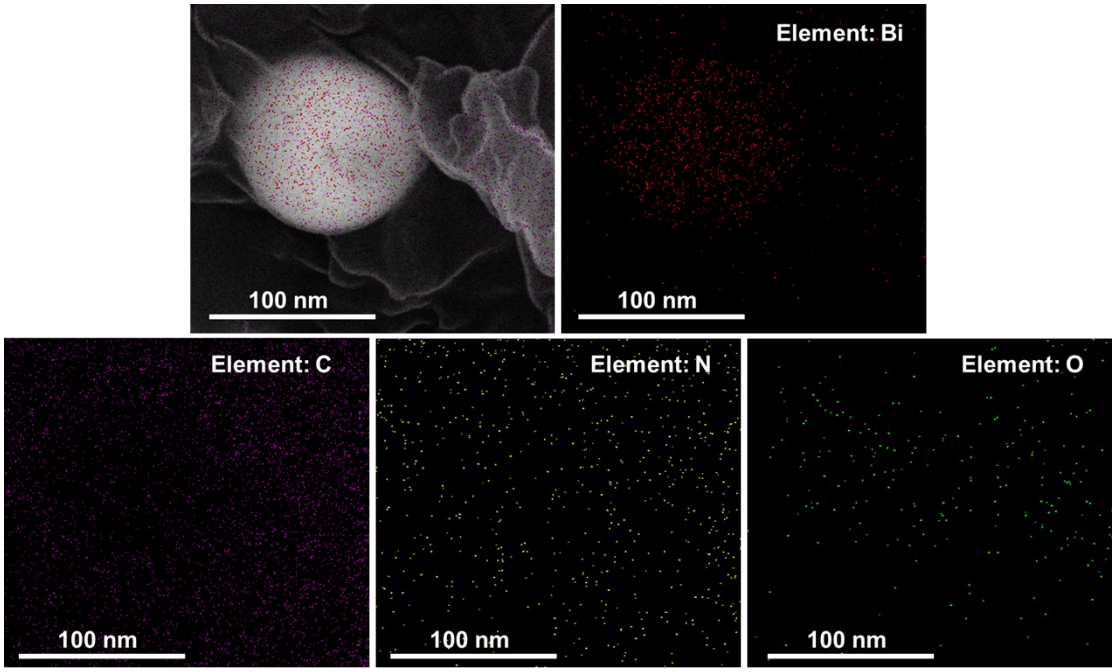

Fig. S5 EDS mapping images of 2% Bi/Bi_2O_3@g-C_3N_4.

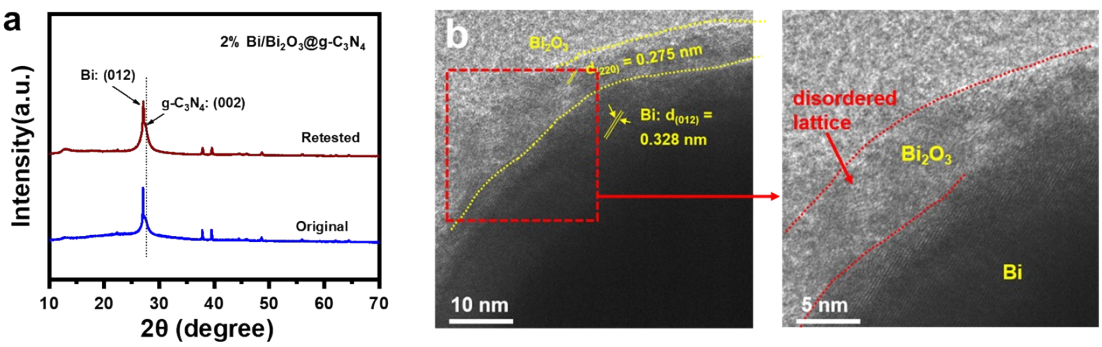

Fig. S6 (a) XRD patterns of original and retested 2% Bi/Bi_2O_3@g-C_3N_4 samples. (b) HRTEM and corresponding magnified region images of 2% Bi/Bi_2O_3@g-C_3N_4.

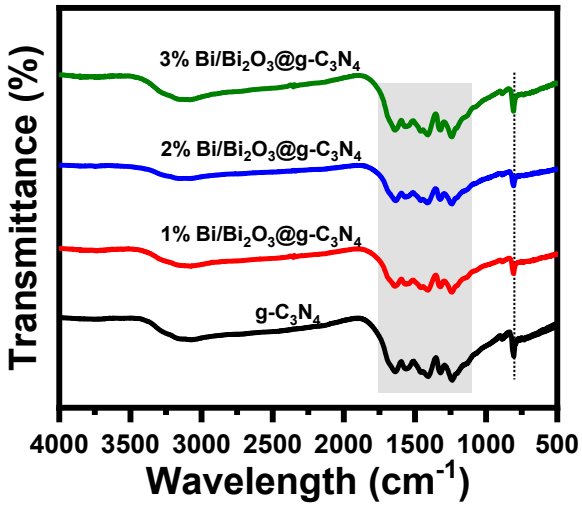

Fig. S7 FTIR spectra of g-C_3N_4, and various Bi/Bi_2O_3@g-C_3N_4 samples.

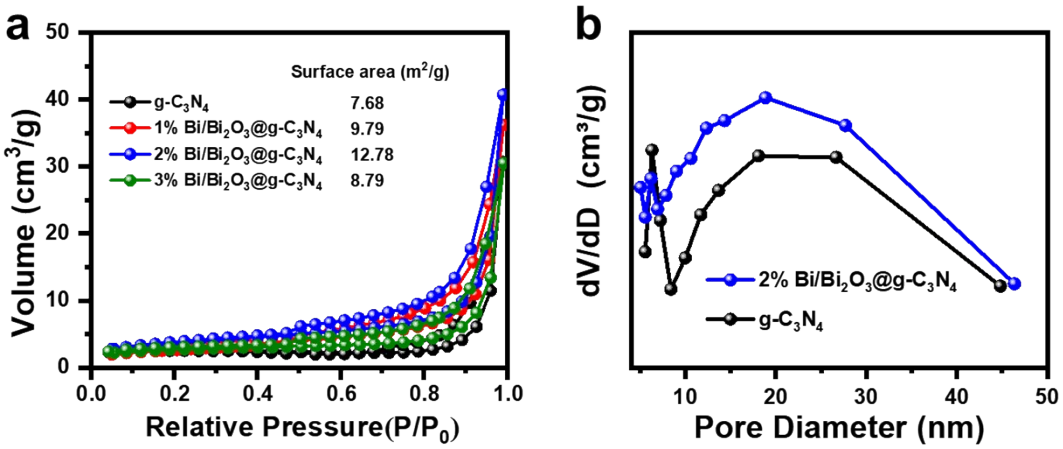

Fig. S8 (a) N_2 adsorption-desorption isotherms of g-C_3N_4, and various Bi/Bi_2O_3@g-C_3N_4 samples. (b) Pore size distribution curves of g-C_3N_4 and 2% Bi/Bi_2O_3@g-C_3N_4 samples.

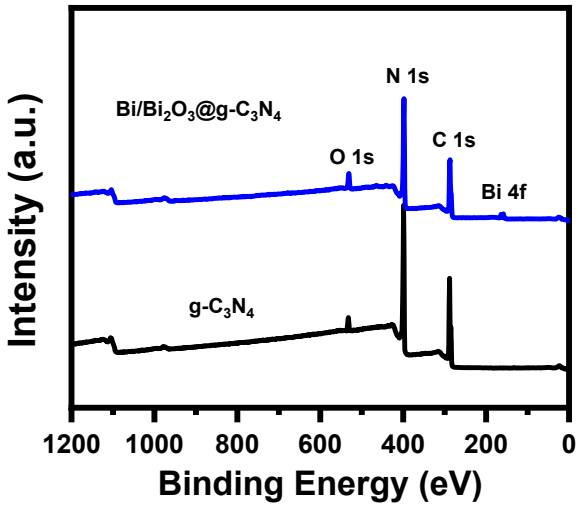

Fig. S9 XPS survey spectra of g-C_3N_4, and 2% Bi/Bi_2O_3@g-C_3N_4 samples.

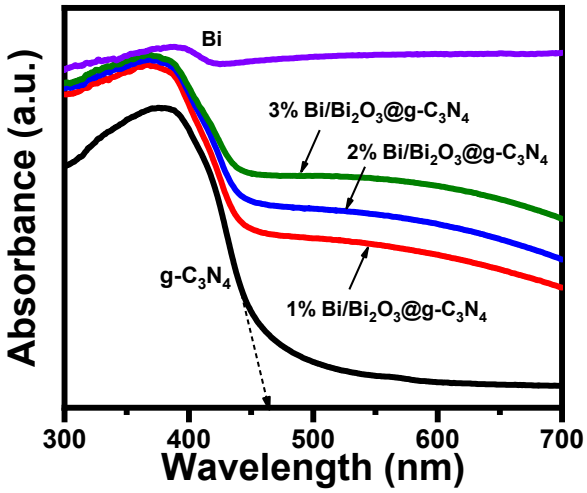

Fig. S10 UV-Vis diffuse reflectance spectra of g-C_3N_4, and various Bi/Bi_2O_3@g-C_3N_4 samples.

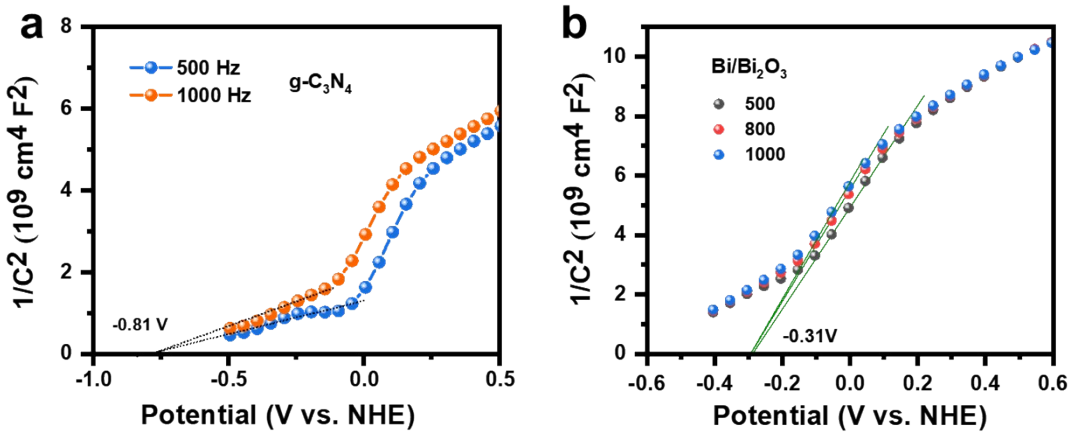

Fig. S11 Mott-Schottky plot of (a) g-C_3N_4 and (b) Bi/Bi_2O_3 at different frequencies.

We used ultraviolet photoelectron spectroscopy (UPS) to determine the Fermi level [*Angew. Chem. Int. Ed.*, 2019, 48, 2-8]. According to the linear intersection method, the work functions (Φ) of g-C_3N_4 and 2% Bi/Bi_2O_3@g-C_3N_4 were calculated to be 3.50 and 4.09 eV (vs vacuum), respectively, by subtracting the width of the He I UPS spectrum from the excitation energy (21.22 eV), as shown in equation of $h\nu = E_{cutoff} + \phi$. Based on the relationship between the vacuum energy (E_{abs}) and the normal electrode potential (E_θ), $E_{abs} = -E_\theta - 4.5$ eV, the Fermi level of the g-C_3N_4 and 2% Bi/Bi_2O_3@g-C_3N_4 were calculated to be -1.0 V and -0.41 V (vs. NHE), respectively.

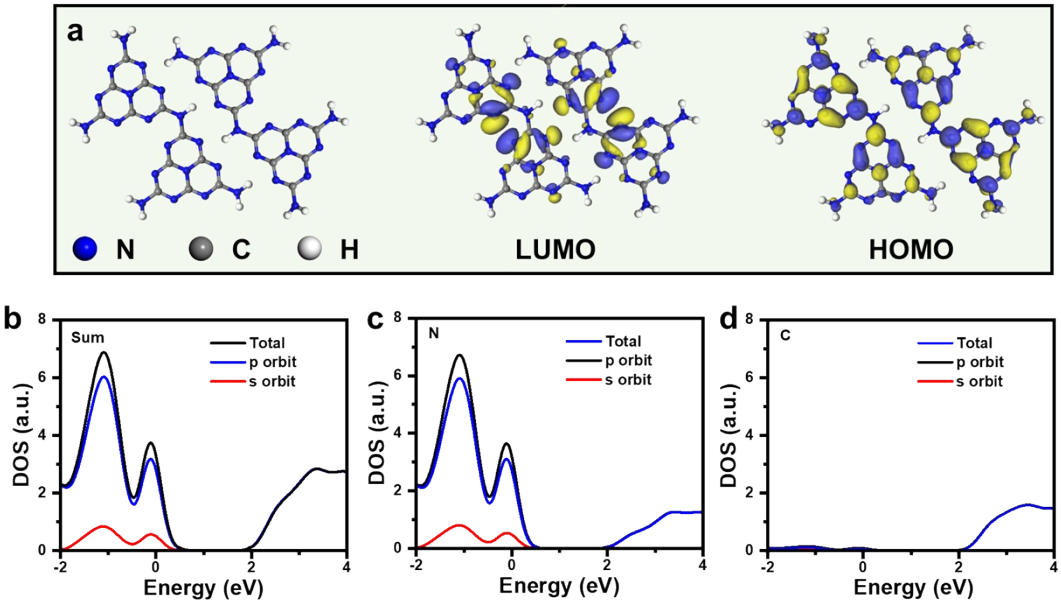

Fig. S12 (a) DFT calculations for the molecular orbits of g-C_3N_4 model (Yellow and blue isosurfaces represent electron accumulation and electron depletion, respectively). Density of states (DOS) of g-C_3N_4 model: (b) sum, (c) N and (d) C elements.

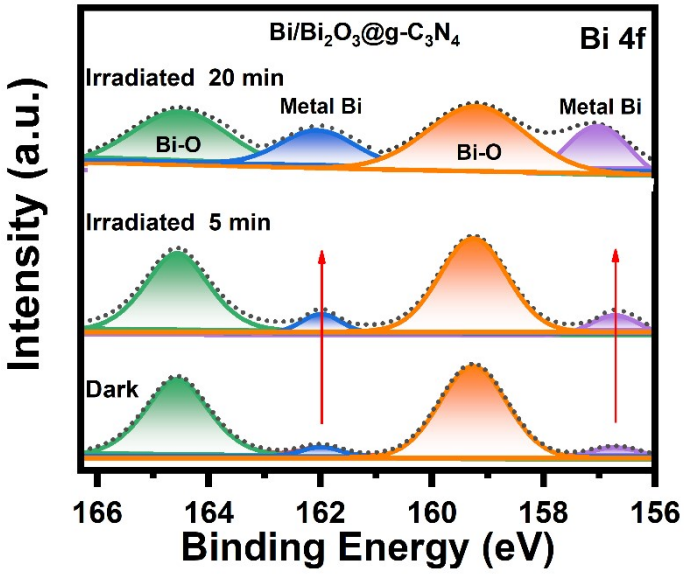

Fig. S13 Bi 4f XPS spectra of 2% Bi/Bi_2O_3@g-C_3N_4 samples in dark, light irradiation for 5 min and 20 min.

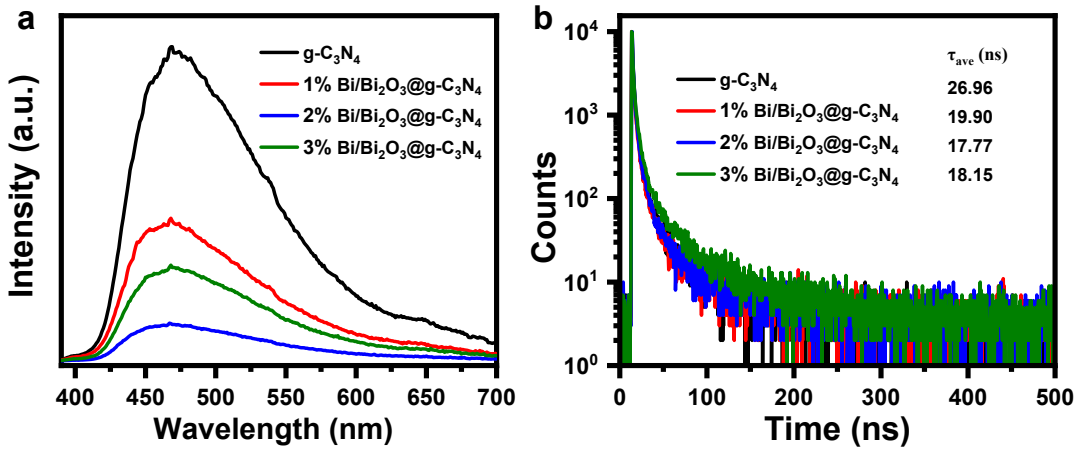

Fig. S14 (a) PL spectra and (b) decay curves of g-C_3N_4, and various Bi/Bi_2O_3@g-C_3N_4 samples.

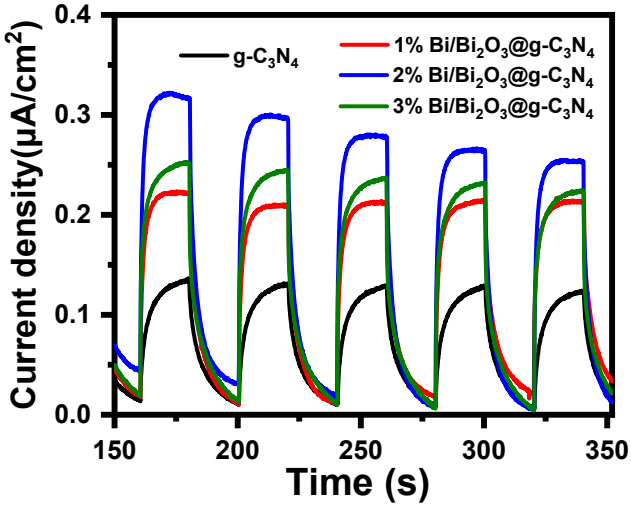

Fig. S15 Time-dependent photocurrent responses of g-C_3N_4, and various Bi/Bi_2O_3@g-C_3N_4 samples.

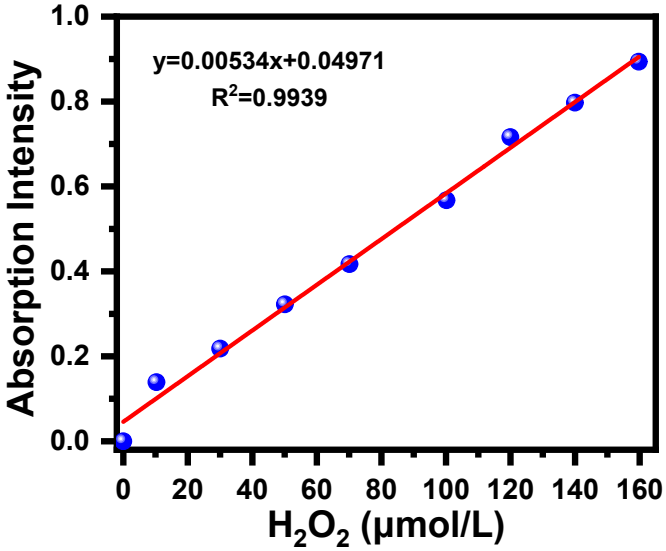

Fig. S16 Standard curve of H_2O_2 evolution amount.

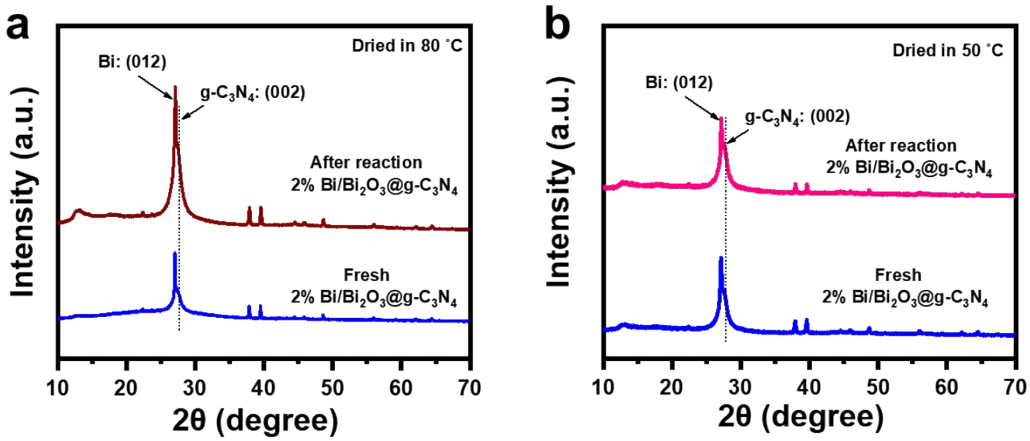

Fig. S17 XRD patterns of fresh and used 2% Bi/Bi_2O_3@g-C_3N_4 samples under the dried temperature of (a) 80 ºC and (b) 50 ºC.

Notes: Fig. S17 shows the enhanced intensity of XRD diffraction peaks of 2% Bi/Bi_2O_3@g-C_3N_4 after reaction, which demonstrates the degree of crystallinity is improved. After photocatalytic reaction, the photocatalyst powder of 2% Bi/Bi_2O_3@g-C_3N_4 was separated by centrifugation and dried in 80 ºC oven for 24 h. It should be considered that the long-time high temperature could lead to the change of crystallinity degree. Considering the temperature element, we retested the photocatalytic reaction using 2% Bi/Bi_2O_3@g-C_3N_4 sample and obtained the dried powder under lower temperature (~50 ºC). The XRD pattern in Fig. S17b shows the intensity of diffraction peaks is appropriate to the fresh 2% Bi/Bi_2O_3@g-C_3N_4.

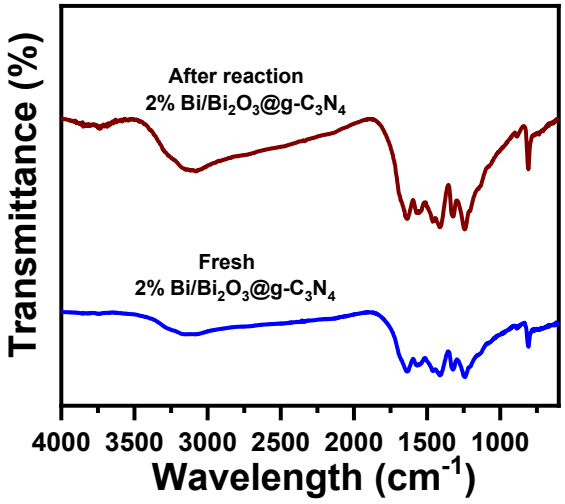

Fig. S18 FTIR spectra of fresh and used 2% Bi/Bi_2O_3@g-C_3N_4 samples.

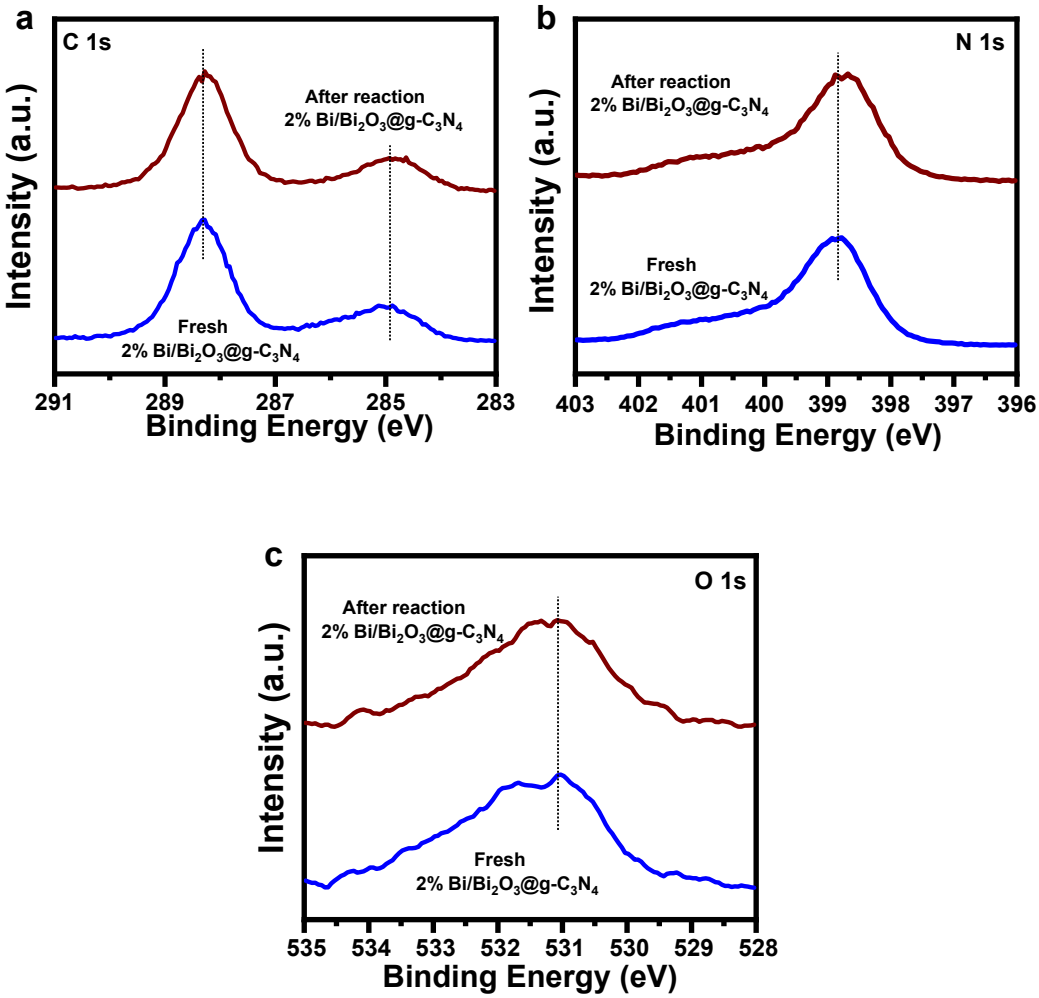

Fig. S19 (a) C 1s, (b) N 1s, and (c) O 1s spectra of fresh and used 2% Bi/Bi_2O_3@g-C_3N_4 samples.

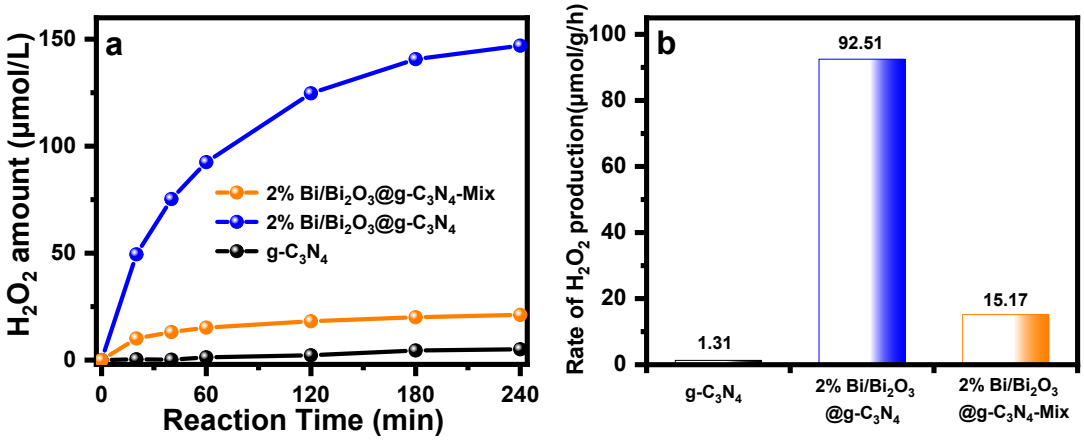

Fig. S20 (a) Time course of photocatalytic H_2O_2 production and (b) H_2O_2 production rate for g-C_3N_4, 2% Bi/Bi_2O_3@g-C_3N_4 and 2% Bi/Bi_2O_3@g-C_3N_4-Mix samples under pure water.

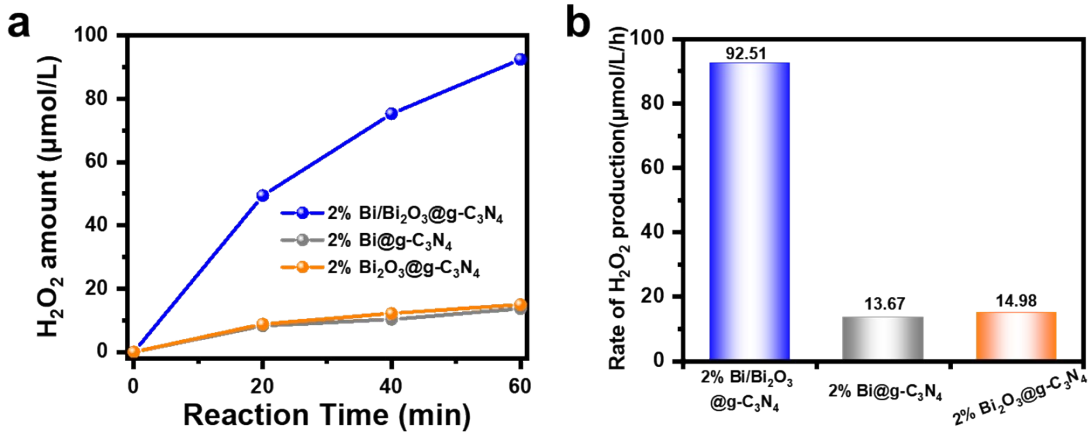

Fig. S21 (a) Time course of photocatalytic H_2O_2 production and (b) H_2O_2 production rate for 2% Bi@g-C_3N_4, 2% Bi_2O_3@g-C_3N_4 and 2% Bi/Bi_2O_3@g-C_3N_4 samples under pure water.

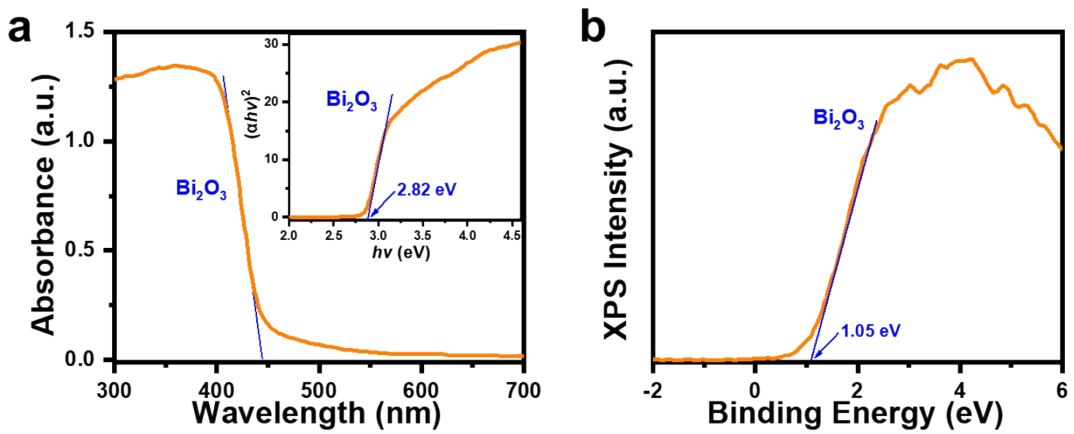

Fig. S22 (a) UV-Vis diffuse reflectance spectra (inset is plots of transformed Kubelka–Munk function versus photon energy), (b) VB-XPS spectra of Bi_2O_3.

Notes: Fig. S22a shows an obvious absorption edge at 444 nm for Bi_2O_3, which corresponds to the bandgap of 2.82 eV. The VB-XPS spectra in Fig. S22b displays the distances from the valance band (VB) to the Fermi level for Bi_2O_3 is estimated to be 1.05 eV. By applying the reported Fermi levels of Bi_2O_3 to be 1.73 eV (vs. NHE) [*J. Mater. Sci. Technol.* **2020,** *52,* 145], the VB position of Bi_2O_3 is determined to be 2.78 eV. Based on the formula $E_g = E_{VB}-E_{CB}$, the conduction band (CB) position of Bi_2O_3 is calculated to be -0.04 eV.

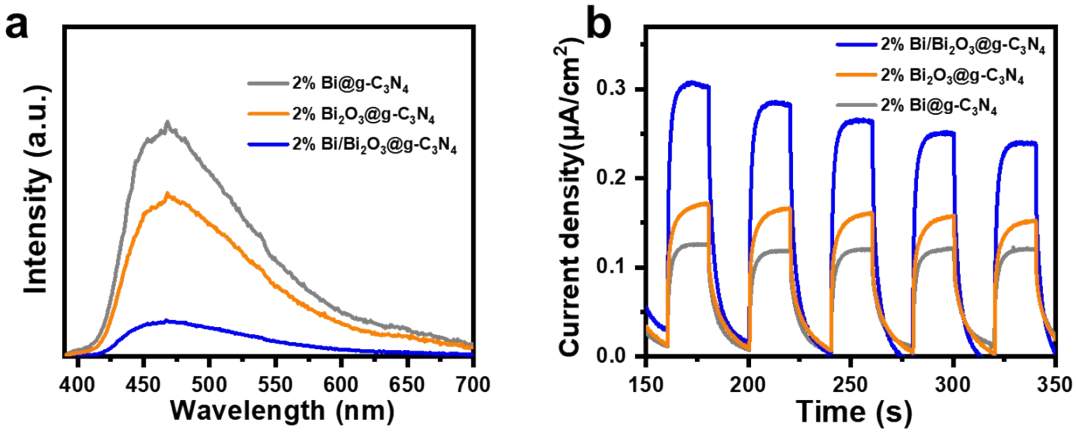

Fig. S23 (a) PL emission spectra and (b) photocurrent curves for 2% Bi@g-C_3N_4, 2% Bi_2O_3@g-C_3N_4 and 2% Bi/Bi_2O_3@g-C_3N_4 samples.

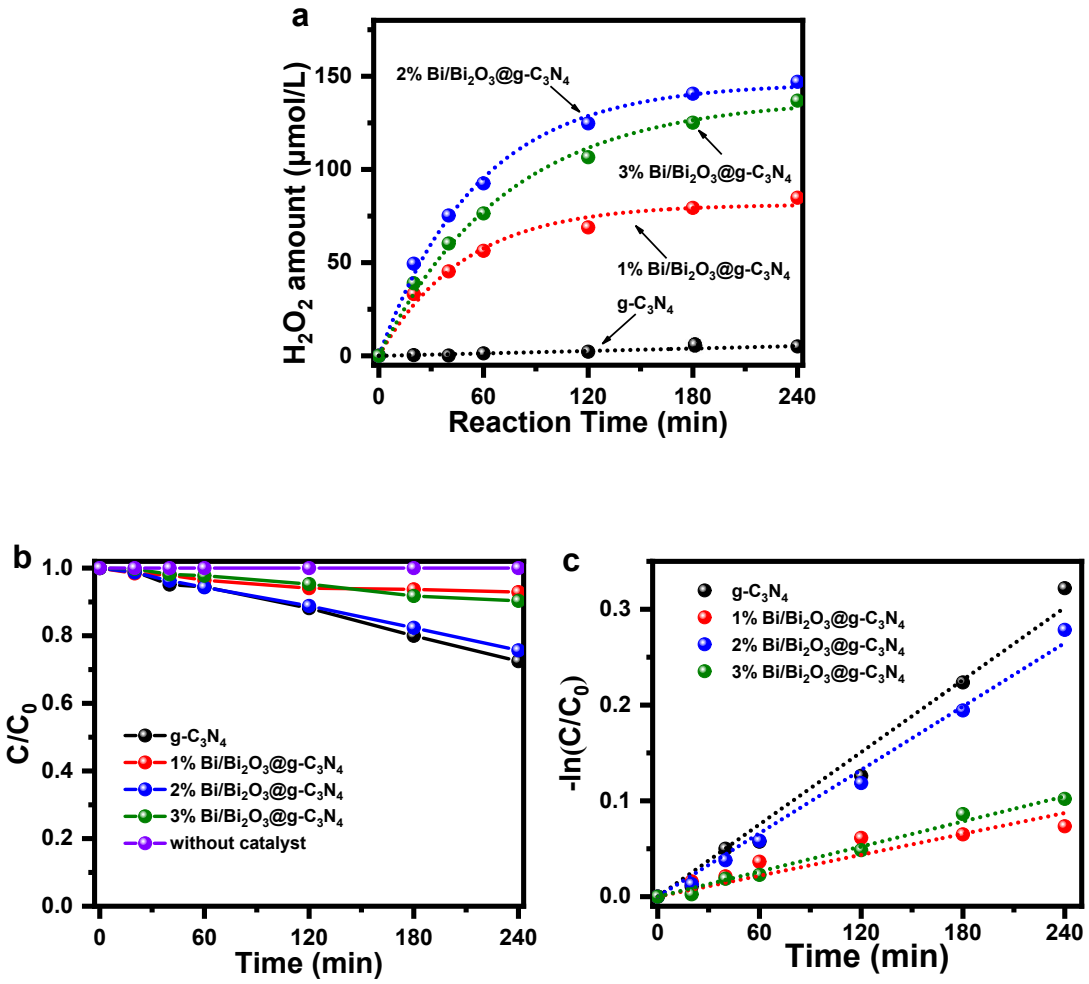

Fig. S24 (a) Zero-order kinetic fitting curves (b, c) first-order kinetic fitting curves of g-C_3N_4, and various Bi/Bi_2O_3@g-C_3N_4 samples.

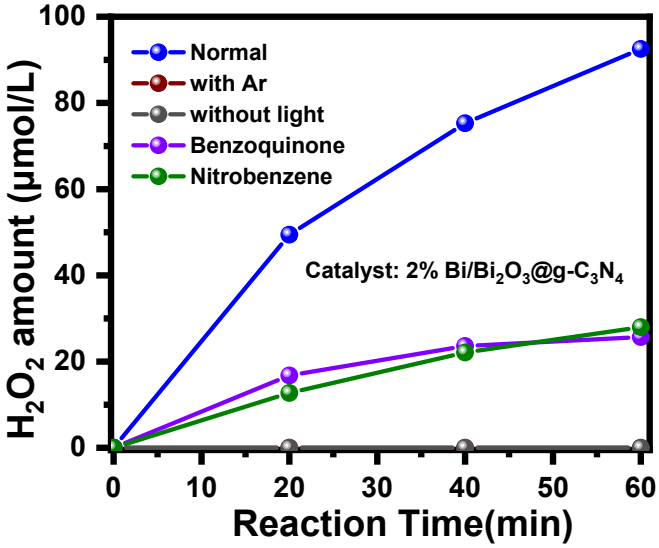

Fig. S25 Time course of photocatalytic H_2O_2 production over 2% Bi/Bi_2O_3@g-C_3N_4 with different quenchers.

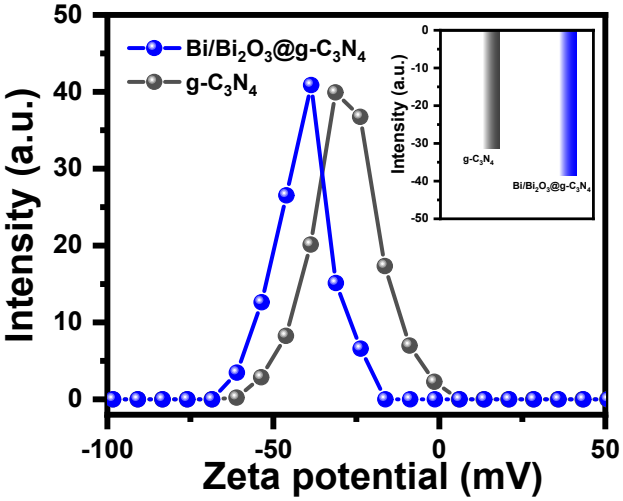

Fig. S26 Comparison of Zeta potentials over pristine g-C_3N_4 and various Bi/Bi_2O_3@g-C_3N_4 samples in pure water.

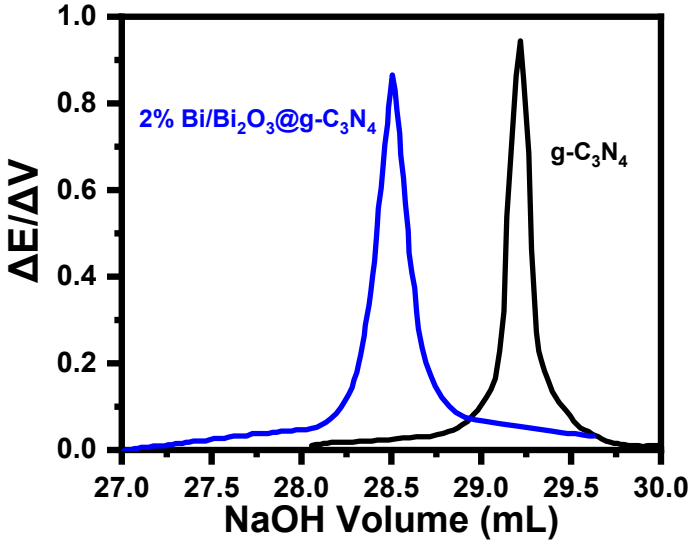

Fig. S27 The first derivative curve of the relationship between $\Delta E/\Delta V$ and titration volume using 10^{-5} mol/L NaOH as the titrant upon g-C_3N_4 and 2% Bi/Bi_2O_3@g-C_3N_4 samples based on potentiometric titration method.

Notes: The detailed experiment process of the potentiometric titration method is described as follows. Pure g-C_3N_4 and Bi/Bi_2O_3@g-C_3N_4 are respectively dispersed into the 10^{-5} mol/L HCl solution (pH=5) with the equal quality (20 mg) and volume (30 mL). The two mixture liquids stirred for 3 h and then kept standing for 24 h. The purpose of these operations is to achieve the adsorption equilibrium between the catalyst surface and H^+. The absorbed solution is obtained via centrifugation and the concentration is determined by potentiometric titration using 10^{-5} mol/L NaOH as the titrant. Fig. S27 shows the first derivative curve of the relationship between $\Delta E/\Delta V$ and titration volume (V, mL). It is seen that the titration volume of Bi/Bi_2O_3@g-C_3N_4 is less than that of g-C_3N_4, which indicates the residual concentration of H^+ is reduced. Fig. S26 shows that Bi/Bi_2O_3@g-C_3N_4 sample possesses more negative surface potential than pure g-C_3N_4 (Zeta potential: -38.6 mV vs. -31.3 mV). Based on the attraction theory between positive and negative charges, the more negative potential of Bi/Bi_2O_3@g-C_3N_4 could adsorb more positive H^+ in solution, which leads to the decreased concentration of residual H^+. Therefore, the peak of titration curve of Bi/Bi_2O_3@g-C_3N_4 is left-shift in comparison with g-C_3N_4.

Table S1 The element content of g-C_3N_4 and 2% Bi/Bi_2O_3@g-C_3N_4 based ICP analysis.

Sample	Element Content (At%)			
	Bi	**C**	**N**	**O**
g-C_3N_4	/	42.9	54.36	2.73
2% Bi/Bi_2O_3@g-C_3N_4	0.12	47.34	47.46	5.08

Table S2 The absolute fluorescence quantum yield (%) of g-C_3N_4 and Bi/Bi_2O_3@g-C_3N_4 samples excited at 340 nm in the wavelength range of 390-550 nm.

Photocatalyst	Absolute fluorescence quantum yield (%)
g-C_3N_4	3.40
1% Bi/Bi_2O_3@g-C_3N_4	2.11
2% Bi/Bi_2O_3@g-C_3N_4	0.82
3% Bi/Bi_2O_3@g-C_3N_4	1.49

Table S3 Time constant τ of fluorescence decay curves of g-C_3N_4 and Bi/Bi_2O_3@g-C_3N_4 samples.

Sample	τ_1	%	τ_2	%	τ_3	%	τ_{ave}
g-C_3N_4	1.20	56.39	5.77	31.34	38.70	12.27	26.96
1% Bi/Bi_2O_3@g-C_3N_4	1.08	64.03	4.78	28.84	33.90	7.13	19.90
2% Bi/Bi_2O_3@g-C_3N_4	1.01	62.06	4.54	30.73	30.82	7.20	17.77
3% Bi/Bi_2O_3@g-C_3N_4	1.10	74.46	5.17	20.78	34.94	4.76	18.15

Table S4 Comparison of H_2O_2 production performance of different photocatalysts.

Photocatalysts	Reaction solution	Dosage (g L^{-1})	Light source	H_2O_2 yield (μmol/L/h)	Reference
g-C_3N_4/PDI	Water (30 mL)	1.67	2 kW XL (λ>420 nm)	35.20	[5]
g-C_3N_4/PDI/rGO	Water (30 mL)	1.67	2 kW XL (λ>420 nm)	40.20	[6]
3DOM g-C_3N_4-PW_{11}	Water (100 mL)	1.00	300 W XL (λ>320 nm)	35.00	[7]
Ag@U-g-C_3N_4-NS	Water (100 mL)	1.00	300 W XL (λ>420 nm)	67.50	[8]
g-C_3N_4-PWO	Water (100 mL)	1.00	300 W XL (λ≥420 nm)	63.00	[9]
Bi/g-C_3N_4	**Water (50 mL)**	**1.00**	**300 W XL (λ≥420 nm)**	**92.50**	**This work**

Reference

[1] P. Hohenberg, W. Kohn, Inhomogeneous electron gas. *Phys. Rev.* **1964,** *136,* B864-B871.

[2] W. Kohn, L-J. Sham, Self-consistent equations including exchange and correlation effects. *Phys. Rev.* **1965,** *104,* A1133-A1138.

[3] J-P. Perdew, K. Burke, M. Ernzerhof, Generalized gradient approximation made simple. *Phys. Rev. Lett.* **1996,** *77,* 3865–3868.

[4] E-R, McNellis, J. Meyer, K. Reuter, Azobenzene at coinage metal surfaces: role of dispersive van der waals interactions. *Phys.Rev. B* **2009,** *80,* 205414.

[5] Shiraishi, Y.; Kanazawa, S.; Kofuji, Y.; Sakamoto, H.; Ichikawa, S.; Tanaka, S.; Hirai, T., Sunlight-Driven Hydrogen Peroxide Production from Water and Molecular Oxygen by Metal-Free Photocatalysts. *Angew. Chem. Int. Ed.* **2014,** *53* (49), 13454-13459.

[6] Kofuji, Y.; Isobe, Y.; Shiraishi, Y.; Sakamoto, H.; Tanaka, S.; Ichikawa, S.; Hirai, T., Carbon Nitride-Aromatic Diimide-Graphene Nanohybrids: Metal-Free Photocatalysts for Solar-to-Hydrogen Peroxide Energy Conversion with 0.2% Efficiency. *J. Am. Chem. Soc.* **2016,** *138*, 10019-10025.

[7] Zhao, S.; Zhao, X.; Zhang, H.; Li, J.; Zhu, Y., Covalent combination of polyoxometalate and graphitic carbon nitride for light-driven hydrogen peroxide production. *Nano Energy* **2017,** *35*, 405-414.

[8] Cai, J.; Huang, J.; Wang, S.; Iocozzia, J.; Sun, Z.; Sun, J.; Yang, Y.; Lai, Y.; Lin, Z., Crafting Mussel-Inspired Metal Nanoparticle-Decorated Ultrathin Graphitic Carbon Nitride for the Degradation of Chemical Pollutants and Production of Chemical Resources. *Adv. Mater.* **2019,** *31*, e1806314.

[9] Peng, Y.; Wang, L.; Liu, Y.; Chen, H.; Lei, J.; Zhang, J., Visible-Light-Driven Photocatalytic H_2O_2 Production on g-C_3N_4 Loaded with CoP as a Noble Metal Free Cocatalyst. *Eur. J. Inorg. Chem.* **2017,** *2017*, 4797-4802.